

## On the time and mechanism of nanoparticle functionalization by macromolecular ligands during pulsed laser ablation in liquids

Alexander Letzel, Stefan Reich, Tomy dos Santos Rolo, Alexander Kanitz, Jan Hoppius, Alexander Rack, Margie Olbinado, Andreas Ostendorf, Bilal Gökce, Anton Plech, and Stephan Barcikowski

*Langmuir*, **Just Accepted Manuscript** • DOI: 10.1021/acs.langmuir.8b01585 • Publication Date (Web): 15 Jan 2019

Downloaded from <http://pubs.acs.org> on January 17, 2019

### Just Accepted

“Just Accepted” manuscripts have been peer-reviewed and accepted for publication. They are posted online prior to technical editing, formatting for publication and author proofing. The American Chemical Society provides “Just Accepted” as a service to the research community to expedite the dissemination of scientific material as soon as possible after acceptance. “Just Accepted” manuscripts appear in full in PDF format accompanied by an HTML abstract. “Just Accepted” manuscripts have been fully peer reviewed, but should not be considered the official version of record. They are citable by the Digital Object Identifier (DOI®). “Just Accepted” is an optional service offered to authors. Therefore, the “Just Accepted” Web site may not include all articles that will be published in the journal. After a manuscript is technically edited and formatted, it will be removed from the “Just Accepted” Web site and published as an ASAP article. Note that technical editing may introduce minor changes to the manuscript text and/or graphics which could affect content, and all legal disclaimers and ethical guidelines that apply to the journal pertain. ACS cannot be held responsible for errors or consequences arising from the use of information contained in these “Just Accepted” manuscripts.



1  
2  
3  
4  
5  
6  
7 On the time and mechanism of nanoparticle  
8  
9  
10  
11 functionalization by macromolecular ligands during  
12  
13  
14  
15 pulsed laser ablation in liquids  
16  
17  
18  
19

20 *Alexander Letzel,<sup>1‡</sup> Stefan Reich,<sup>2‡</sup> Tomy dos Santos Rolo,<sup>2</sup> Alexander Kanitz,<sup>3</sup> Jan Hoppius,<sup>3</sup>*  
21  
22 *Alexander Rack,<sup>4</sup> Margie Olbinado,<sup>4</sup> Andreas Ostendorf,<sup>3</sup> Bilal Gökce,<sup>1\*</sup> Anton Plech,<sup>2\*</sup> and*  
23  
24 *Stephan Barcikowski<sup>1</sup>*  
25  
26  
27

28 <sup>1</sup> Department of Technical Chemistry I and Center for Nanointegration Duisburg-Essen  
29  
30 (CENIDE), University of Duisburg-Essen, Universitätsstr. 7, 45141 Essen, Germany  
31  
32

33 <sup>2</sup> Institute for Photon Science and Synchrotron Radiation, Karlsruhe Institute of Technology  
34  
35 (KIT), Hermann-von-Helmholtz-Platz 1, 76344 Eggenstein-Leopoldshafen, Germany  
36  
37

38 <sup>3</sup> Applied Laser Technologies, Ruhr-University Bochum, Universitätsstr. 150, 44801 Bochum,  
39  
40 Germany  
41

42 <sup>4</sup> European Synchrotron Radiation Facility (ESRF), 30843 Grenoble, France  
43  
44  
45  
46  
47

48 **KEYWORDS**  
49  
50

51 X-ray imaging; Hartmann mask; Laser ablation synthesis in solution; Size quenching; In situ  
52  
53  
54  
55  
56  
57  
58  
59  
60

## ABSTRACT

Laser ablation of gold in liquids with nanosecond laser pulses in aqueous solutions of inorganic electrolytes and macromolecular ligands for gold nanoparticle size quenching is probed inside the laser-induced cavitation bubble by *in situ* X-ray multi-contrast imaging with a Hartmann mask (XHI). It is found that (i) the *in situ* size quenching power of sodium chloride (NaCl) in comparison to the ablation in pure water can be observed by the scattering contrast from XHI already inside the cavitation bubble, while (ii) for polyvinylpyrrolidone (PVP) as a macromolecular model ligand an *in situ* size quenching cannot be observed. Complementary *ex situ* characterization confirms the overall size quenching ability of both additive types NaCl and PVP. The macromolecular ligand as well as its monomer N-vinylpyrrolidone (NVP) are mainly effective for growth quenching of larger nanoparticles on later time scales, leading to the conclusion of an alternative interaction mechanism with ablated nanoparticles compared to the electrolyte NaCl, probably outside of the cavitation bubble, in the surrounding liquid phase. While monomer and polymer have similar effects on the particle properties, with the polymer being slightly more efficient, only the polymer is effective against hydrodynamic aggregation.

## INTRODUCTION

Since the discovery of pulsed laser ablation in liquids (LAL) as a tool for the synthesis of nanoparticles in 1993 [1] researchers still face major challenges that hinder LAL from being established as a competitive synthesis route towards nanomaterials [2]. Two of these are the control of mean size, and size distribution width. The challenge of gaining control over the final

1  
2  
3 nanoparticle size in a single-step approach and without using surfactants or ligands was  
4  
5 accelerated by the discovery that micromolar concentrations of monovalent salts like sodium  
6  
7 chloride (NaCl) result in a size quenching of gold nanoparticles by adsorption to the particle  
8  
9 surface and stronger electrostatic stabilization [3, 4]. This approach was extended to other noble  
10  
11 metals like palladium [5] and platinum [6]. It was found recently that size reduction by ions  
12  
13 already happens inside the gas phase [7] of the laser-induced cavitation bubble [8-10] some tens  
14  
15 of microseconds after a laser pulse hits the target [7]. Ions present in the electrolyte get in contact  
16  
17 very early to the plasma emitted from the target and are thus able to interact with the material  
18  
19 even before bubble expansion [11]. Note that Sakka et al. [12] demonstrated the presence of  
20  
21 dissolved ions already in the laser-induced plasma. However, they used 100 ns laser pulse width,  
22  
23 we used only 10 ns, and it cannot be excluded that ions are present inside the bubble because of  
24  
25 solution vaporization at the plasma edge during its lifetime. Trapping of the early nanoparticles  
26  
27 inside the confinement of the cavitation bubble had been observed first by means of time-  
28  
29 resolved scanning small-angle X-ray scattering (SAXS) [13]. In the last years, a trend towards  
30  
31 imaging of the entire bubble cross section by optical [14, 15] and *in situ* X-ray methods was  
32  
33 followed. In this context X-ray radiography and multi-contrast imaging [16, 17] was introduced  
34  
35 as a complement to *in situ* SAXS [18, 19]. Thereby, the distribution of nanoparticles and the  
36  
37 ejection time of nanoparticles from the gaseous phase into the surrounding liquid were  
38  
39 determined exploiting X-ray absorption contrast [18].  
40  
41  
42  
43  
44  
45  
46  
47

48 Alternative to anions, organic molecules can be employed for size quenching *in situ* [20-22], in  
49  
50 particular, if the ligand's functional group has high affinity to the inorganic nanoparticle surface  
51  
52 [23-25]. But less is known on the size quenching mechanism with macromolecules having no  
53  
54 specific anchor group.  
55  
56  
57  
58  
59  
60

1  
2  
3 In this work, we address the controversy of the actual temporal and spatial distribution of LAL  
4 nanoparticles in the presence of macromolecular ligands to interact during *in situ* conjugation.  
5  
6 This question was addressed by other groups by adding ligands like sodium dodecyl sulfate  
7  
8 (SDS) [26] or 2-[2-(2-methoxyethoxy)ethoxy] acetic acid (MEEAA) [27] to the water phase.  
9  
10 While these studies provides indication for particle-ligand interaction during an early stage, the  
11  
12 size quenching cannot be solely attributed to the presence of the organic backbone as both SDS  
13  
14 and MEEAA introduce additional electrolytes or change the pH of the liquid [5]. Steric  
15  
16 stabilization and size reduction by polymers added to the liquid prior to laser ablation was  
17  
18 observed for ,e.g., aluminum nanoparticles prepared in poly(vinyl alcohol) (PVA) solution [28],  
19  
20 gold nanoparticles in poly(ethylene oxide) (PEG) solution [20] and silver nanoparticles in  
21  
22 polyvinylpyrrolidone (PVP) solution [29]. The present study focuses on the functionalization of  
23  
24 LAL nanoparticles by PVP. Tsuji et al. have demonstrated that PVP acts as a size quenching  
25  
26 ligand in LAL using silver as a target material [29]. In chemical reduction synthesis of silver and  
27  
28 gold nanoparticles PVP acts as a shape directing agent in some formulations [30, 31] and the  
29  
30 same is true for materials like palladium and tellurium [32]. Yet the chemical synthesis of gold  
31  
32 nanoparticles with PVP is reported frequently, while spherical morphologies are found [33-36].  
33  
34 Requejo et al. have even reported a route in which PVP leads to spherical gold particles and the  
35  
36 omission of PVP results in gold nanorods [37]. Non-spherical nanoparticles were also found  
37  
38 during laser processing of nanoparticles when using a 355 nm laser source and performing laser  
39  
40 fragmentation [38], these parameters and the setup are, however, not completely transferrable to  
41  
42 those applied in this work.  
43  
44  
45  
46  
47  
48  
49  
50

51  
52 As a matter of fact, it is possible to control the size of gold nanoparticles to some extent by a  
53  
54 controlled delayed addition of oligonucleotides to the colloidal solution [39, 40]. This indicates  
55  
56  
57  
58  
59  
60

1  
2  
3 that quenching by organic ligands can occur *ex situ*, i.e. outside of the cavitation bubble, by  
4  
5 suppressing growth processes like Ostwald ripening and coagulation by steric stabilization of the  
6  
7 nanoparticles [41]. Accordingly, there is indication for both possible quenching mechanisms,  
8  
9 inside and outside of the cavitation bubble, occurring during LAL in the presence of  
10  
11 macromolecular ligands. Therefore, it is mandatory to study nanoparticle formation during an  
12  
13 early phase as well, when particles are still trapped inside the cavitation bubble. Due to the  
14  
15 complexity of the problem a complementary approach to our earlier *in situ* SAXS studies is  
16  
17 chosen [7, 13, 18, 42]. X-ray Hartmann mask imaging (XHI) was utilized to access multicontrast  
18  
19 X-ray imaging, including scattering contrast [43, 44]. As described earlier in literature [43, 45-  
20  
21 47] Hartmann-mask imaging exploits a laterally structured X-ray beam, whose attenuation,  
22  
23 pattern shift and structure broadening allows to decompose absorption, differential phase and  
24  
25 scattering contrast on a 2D detector. Here, the Hartmann mask consists of a platinum foil with a  
26  
27 2D periodic pattern of holes as shown in Figure 1a-d. The sensitivity maximum of targeted size  
28  
29 intervals can be set by variation of the mask pitch and the sample to detector distance [45]. We  
30  
31 have chosen a XHI setup with sensitivity maximum at 55 nm structure size. Hence, secondary  
32  
33 particles like large spherical nanoparticles and agglomerates are preferably detected over smaller  
34  
35 (primary) particles.  
36  
37  
38  
39  
40  
41  
42  
43  
44  
45

## 46 EXPERIMENTAL SECTION

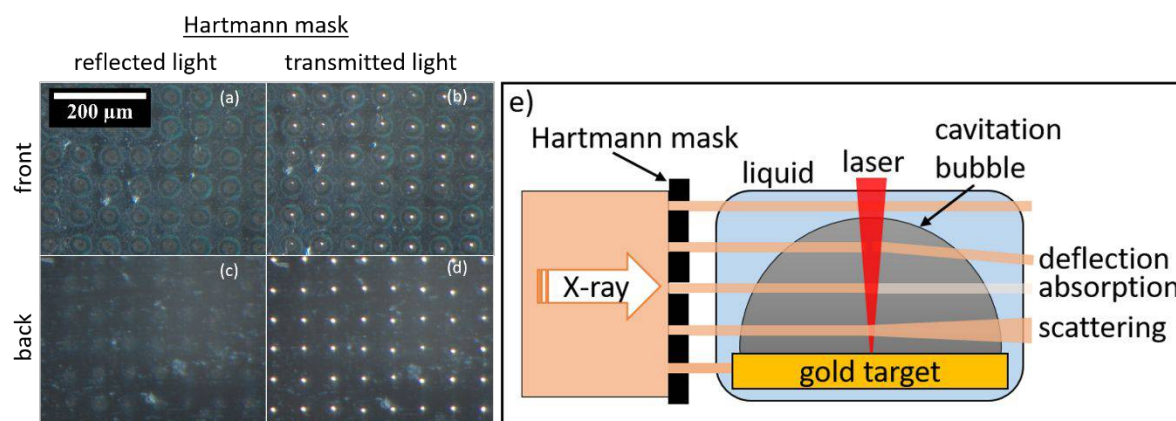
47  
48  
49 The experimental details of the liquid-flow *in situ* LAL setup are described elsewhere in more  
50  
51 detail [7, 19, 42]. In brief, laser ablation for *in situ* experiments was performed by focusing a  
52  
53 nanosecond laser (Continuum Minilite I, 1064 nm, 7 ns, 10 Hz) with an average pulse energy of  
54  
55  
56  
57  
58  
59  
60

1  
2  
3 11 mJ onto the target [19]. The effective fluence, taking the attenuation of the liquid layer at the  
4 laser wavelength into account [48], was 33 J/cm<sup>2</sup>. A gold ribbon (99.9 %) having a width of  
5  
6 4 mm and a thickness of 200 μm was used as a target material and continuously transported  
7  
8 upwards through the chamber in the same direction as the liquid flow. Ablation was performed in  
9  
10 a liquid flow configuration to remove residual nanoparticles for subsequent laser shots. Doubly-  
11  
12 distilled water solutions of NaCl and PVP (Acros Organics, 3,500 g/mol, K12, Lot: A0368382)  
13  
14 were prepared to a final concentration of 0.5 mM. *Ex situ* LAL was performed using a liquid-  
15  
16 flow ablation chamber with a liquid height of 5 mm above the target. A fixed gold plate of  
17  
18 0.5 mm thickness was used. *Ex situ* experiments were additionally conducted in N-  
19  
20 vinylpyrrolidone (NVP), the monomer of PVP. The chemical was obtained from Acros Organics  
21  
22 (99 %, stabilized with NaOH) and used without further purification. Measurements of the pH  
23  
24 value of 1 μM and 1000 μM solutions of NVP revealed that it was almost constant from 5.9 at 1  
25  
26 μM and 5.9-6.0 at 1000 μM. Furthermore, the electrolytic conductivity was constant at 0.7-0.8  
27  
28 μS/cm. The liquid volume flow was 50 ml/min, which is three times lower compared to the *in*  
29  
30 *situ* experiments. For *ex situ* experiments Milli-Q water was used (18.2 MΩ/cm). The laser  
31  
32 (Rofin Sinar RS-Marker 100D, 1064 nm, 10 ns) was operated at 5 mJ pulse energy and 3 kHz  
33  
34 and was scanned across the target surface in a spiral pattern using a galvanometric scanner. The  
35  
36 effective fluence was 27 J/cm<sup>2</sup> which is 18 % less as compared to the *in situ* ablation  
37  
38 experiments. To prove that this slight deviation does not affect the particle size distributions  
39  
40 significantly additional size distributions obtained by *ex situ* LAL using an effective fluence of  
41  
42 36 J/cm<sup>2</sup> are compared with those obtained at 27 J/cm<sup>2</sup> in Figure S1. The ablation chamber was  
43  
44 made out of polytetrafluorethylene (PFTE) to avoid contamination of the product colloids by  
45  
46 ions that might otherwise be dissolved of chambers made of e.g., steel or aluminum. For  
47  
48  
49  
50  
51  
52  
53  
54  
55  
56  
57  
58  
59  
60

1  
2  
3 transmission electron microscopy (TEM) (Zeiss EM 910, 120 kV) the colloids were drop-casted  
4 onto a carbon-coated copper grid. Automatic image analysis was performed by the ImageJ  
5 (Version 1.51s) plugin ParticleSizer [49]. Analytical disc centrifugation (ADC, CPS instruments)  
6 was performed in a sugar density gradient and constantly operated at maximum speed of  
7 24,000 rpm. Gold nanoparticles of 6 nm hydrodynamic diameter were used as calibration  
8 standard. In ADC the integral intensity of the entire injected sample mass is calculated by Mie  
9 theory and from the derived cumulative surface-weighted size distribution the specific surface  
10 area is accessible. Hence, for each data point the additive concentration per nanoparticle surface  
11 area or mass in  $\mu\text{mol}/\text{cm}^2$  or  $\mu\text{mol}/\text{mg}$  is derived, respectively. Note that the specific surface area  
12 and the median diameter are mutually linked quantities. Still, the specific surface area integrates  
13 every size fraction within the size distribution of the gold colloids as every particle contributes to  
14 the overall specific surface area. UV/Vis extinction spectroscopy was performed using a  
15 spectrophotometer (Thermo Scientific Evolution 201). Spectroscopy was used to calculate the  
16 ablated gold mass from the concentration of the *ex situ* synthesized colloids. Representative  
17 spectra from gold nanoparticles produced in pure water, 0.5 mM NaCl and PVP solutions and the  
18 calibration of the UV/Vis spectra by gravimetric analysis of the ablated gold mass are given in  
19 Figure S2. Viscosities were measured using a rheometer (Anton Paar, Physica MCR 301).  
20  
21  
22  
23  
24  
25  
26  
27  
28  
29  
30  
31  
32  
33  
34  
35  
36  
37  
38  
39  
40  
41  
42

43 Time-resolved visible-light shadowgraph of the cavitation bubbles in water and PVP solution  
44 were performed in a self-designed 3D-printed ablation chamber made of acrylonitrile butadiene  
45 styrene. A liquid flow rate of 35 ml/min was applied to remove residual nanoparticles and  
46 persistent bubbles between two laser pulses. The laser repetition rate was set to 0.2 Hz.  
47  
48 Additional information on the used shadowgraphy setup is presented in the Supporting  
49 Information, including the recorded image sequences (Fig. S3-S6).  
50  
51  
52  
53  
54  
55  
56  
57  
58  
59  
60

1  
2  
3 The platinum-based Hartmann mask used for multi-contrast X-ray imaging consists of a 25  $\mu\text{m}$   
4 thick foil (Chempur, 99.9%) with regular holes of about 10  $\mu\text{m}$  in diameter, drilled by pulsed fs-  
5 laser micromachining (Spectra Physics Spitfire Ace, 800 nm, 100 fs) using a fluence of 2 J/cm<sup>2</sup>  
6 at a repetition rate of 5 kHz. The holes cover the rectangular pattern (7x5 mm) with a pitch of  
7 65  $\mu\text{m}$ . Micrographs of the Hartmann mask are shown in Figure 1 from the front and back side.  
8 Light microscopy allows to visualize the funnel shape of the holes on the front side,  
9 perpendicular to the incident transmitted fs-laser (Fig. 1a,b). The back side of the mask does not  
10 exhibit any funnels but a regular pattern of micron sized holes (Fig. 1c,d). A scheme depicting  
11 the basics of the exploited imaging technique for *in situ* measurements during LAL is given in  
12 Figure 1e. Absorption of X-rays occurs whenever a beamlet, shaped by the shadow mask,  
13 interacts with matter e.g., after transmission through water. Transmission increases at the  
14 occurrence of the cavitation bubble in LAL with respect to the surrounding liquid.  
15  
16  
17  
18  
19  
20  
21  
22  
23  
24  
25  
26  
27  
28  
29  
30  
31



46 **Figure 1.** Images of the Pt foil acting as a Hartmann mask for *in situ* experiments obtained by  
47 optical microscopy. Front of the mask in reflected (a) and transmitted light mode (b). The laser-  
48 drilled holes are funnel-shaped on the front side (side at which the laser beam impinges). Back of  
49 the mask in reflected (c) and transmitted light mode (d). Sketch of the XHI approach with the  
50 incoming X-ray beam being split into multiple beamlets by the Hartmann mask, and undergoing  
51  
52  
53  
54  
55  
56  
57  
58  
59  
60

1  
2  
3 absorption, differential phase shift (deflection) and diffuse scattering (broadening) when crossing  
4  
5 the cavitation bubble and the confined nanoparticles (e).  
6  
7  
8  
9

10  
11 XHI experiments were performed at the ID19 beamline of the European Synchrotron Radiation  
12  
13 Facility (ESRF, Grenoble, France) using a quasi-monochromatic beam from a single-line  
14  
15 undulator with an energy of 17.9 keV. The X-ray beam was restricted to an area of 7x5 mm by  
16  
17 slits to illuminate only the Hartmann mask. The array of beamlets formed by the Hartmann mask  
18  
19 passes the sample cell of 5 mm water to be converted to visible light by a YAG scintillator of  
20  
21 100  $\mu\text{m}$  thickness. The distance between the ablation point and the scintillator was 30 mm. A fast  
22  
23 CMOS camera (PCO dimax) recorded the intensity distribution with 40  $\mu\text{s}$  exposure time, a  
24  
25 sequence of images around the ablation event spaced 100  $\mu\text{s}$  was taken. An interleaving of several  
26  
27 films with shifted delay time between acquisition and the laser impact allowed to construct a movie  
28  
29 with 40 kHz (25  $\mu\text{s}$  spacing) image rate. A repetition of the image acquisition for a total of at least  
30  
31 3,000 laser shots was performed for every liquid in order to increase the signal-to-noise ratio. XHI  
32  
33 is a multi-contrast X-ray imaging technique. Details on image formation and reconstruction are  
34  
35 described in detail in [16, 43, 44, 50, 51]. Therefore, here only a short description shall be given.  
36  
37  
38  
39  
40 By usage of a Hartmann mask the intensity, position and broadening of the beamlets reveals three  
41  
42 different contrast modes (absorption, differential phase, and scattering, respectively). In this  
43  
44 publication the scattering contrast is of central interest as this stems from nanoscale  
45  
46 inhomogeneities. The image reconstruction was performed identically to a previous publication by  
47  
48 Reich et al. [51]. Instead of individual beamlet analysis a Fourier transform of the beamlet pattern  
49  
50 allows to separate the different contrasts. Therefore, the Fourier transform of the pattern is  
51  
52 followed by a back transform of the specific harmonics of the Fourier spectrum. Particularly, the  
53  
54  
55  
56  
57  
58  
59  
60

1  
2  
3 cavitation bubble creates absorption contrast, which imprints on the scattering channel [50]. As  
4 reported earlier, this crosstalk from the absorption contrast to the scattering contrast can be  
5 removed by a decorrelation procedure [51, 52].  
6  
7  
8  
9

## 10 11 12 13 14 RESULTS AND DISCUSSION 15

16  
17 The goal of the present study is to clarify the mechanism of nanoparticle-macromolecular  
18 ligand interaction during LAL. Here, we use (i) pure water as a negative (null effect) reference  
19 liquid, (ii) NaCl (aq.) as positive reference. NaCl has the ability to quench the size of  
20 nanoparticles already inside the gaseous phase of the cavitation bubble, as shown before by  
21 scanning SAXS [7]. The additive (iii) that is employed is the macromolecular ligand PVP. It is  
22 utilized in the exact same molar concentration as NaCl to ensure direct comparability of the  
23 molar size quenching efficiencies. As PVP does not contain mercapto groups (-SH), no covalent  
24 bond (chemisorption) to the gold nanoparticle surface is expected. Yet, the N-C=O groups of the  
25 PVP backbone bind to the gold surface by physisorption [53-55]. Although PVP is frequently  
26 used as a stabilizing ligand for silver [29, 30, 56] rather than gold [35] nanoparticles, a gold  
27 target is used here. This is motivated by gold nanoparticles proving to be effectively quenched by  
28 NaCl [7]. It is shown that NaCl exhibits the ability to quench the size of gold nanoparticles  
29 already inside the cavitation bubble (i.e. *in situ*).  
30  
31  
32  
33  
34  
35  
36  
37  
38  
39  
40  
41  
42  
43  
44  
45  
46  
47

48 Using absorption contrast, it is possible to record the cavitation bubble as shown in the inset of  
49 Figure 2b. Scattering contrast is a result of diffuse scattering of X-rays and originates from  
50 scattering at inhomogeneities of the probed specimen [45]. The angular width of scattering scales  
51 inversely to the object size according to the principles of small-angle X-ray scattering [46, 57].  
52  
53  
54  
55  
56  
57  
58  
59  
60

1  
2  
3 In the present setup the sensitivity ranges from 20-230 nm in sizes (at 50 %, with a maximum at  
4 55 nm). The calculated sensitivity curve is shown in Figure 2a, which was calculated from our  
5  
6  
7  
8  
9  
10  
11  
12  
13  
14  
15  
16  
17  
18  
19  
20  
21  
22  
23  
24  
25  
26  
27  
28  
29  
30  
31  
32  
33  
34  
35  
36  
37  
38  
39  
40  
41  
42  
43  
44  
45  
46  
47  
48  
49  
50  
51  
52  
53  
54  
55  
56  
57  
58  
59  
60

In the present setup the sensitivity ranges from 20-230 nm in sizes (at 50 %, with a maximum at 55 nm). The calculated sensitivity curve is shown in Figure 2a, which was calculated from our setup parameters according to the equation derived by Lynch et al. (equation (68)) [45]. The detection of small primary particles ( $d < 15$  nm) by using XHI is negligible, and primary particle size shifts by the addition of NaCl are also not detected by SAXS [7] because SAXS is limited in differentiation of overlapping size fractions [58]. Hence, for the scope of the present study, the secondary size fraction is the main region of interest, as it is known to be connected to the product colloids' bimodality. The shifted sensitivity towards particles even larger than 100 nm adds complementary information on earlier works. In general, imaging offers prospects to map spatial distributions as opposed to localized SAXS. Within our sensitivity limit we see a homogenous scattering distribution across the bubble. At the same time size information in the classical sense in XHI is lost, therefore size quenching (of large particles) is translated to intensity changes. Anyway, also *in situ* SAXS does not reveal changes in the size of small primary particles induced by NaCl inside the cavitation bubble (Fig. S7).

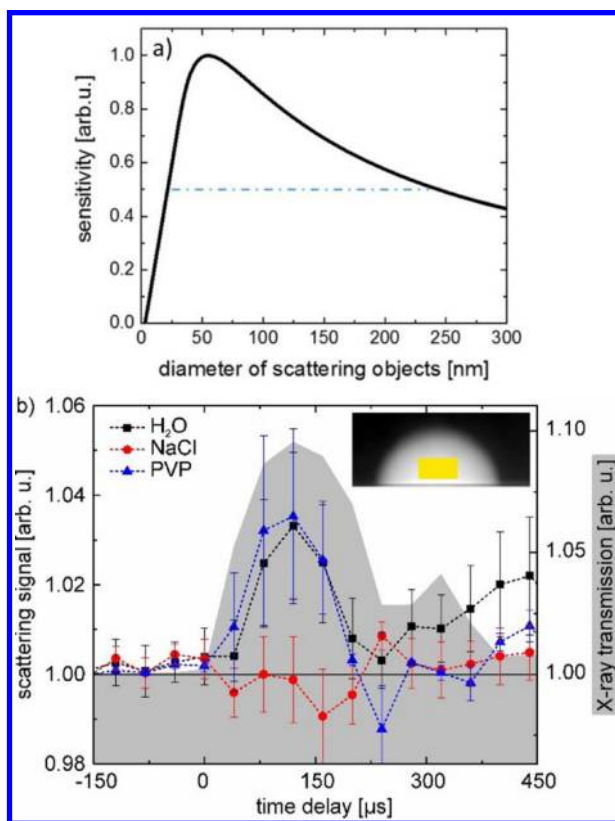


**Figure 2.** Scattering sensitivity on nanoparticles as function of the scattering object size for the given setup. The blue dashed-dotted line indicates the size interval above 50 % relative sensitivity (a). Scattering signal as function of the delay after laser impact obtained at the center of the cavitation bubble (inset shows the transmission signal together with the region of interest) (b). Scattering signals of gold nanoparticles in pure water (black squares), NaCl- (red circles) and PVP-solution (blue triangle) (both 0.5 mM). The shaded curve represents the change in X-ray transmission starting from 1 (0 % intensity change) before laser arrival. Error bars are the standard deviation between several runs.

By using negative delays (before laser impact) for the flat field correction, it is possible to remove signal from residual nanoparticles inside the ablation chamber volume that may not be transported off by the water flow. As visible from the black squares in Figure 2b the scattering

1  
2  
3 signal of gold nanoparticles as ablated in pure water observed at the center of the cavitation  
4 bubble (inset) follows the growth and shrinking of the first and second cavitation bubble, the  
5  
6 latter frequently referred to as bubble rebound. The relation of the cavitation bubble and the  
7  
8 confined particles ablated in pure water further confirms (i) that the observed secondary  
9  
10 nanoparticles are confined within the gaseous phase of the cavitation bubble and (ii) are retracted  
11  
12 towards the target surface upon bubble shrinkage. Therefore, the first reference measurement of  
13  
14 gold nanoparticles in pure water proves the validity of XHI for nanoparticle detection during  
15  
16 LAL by reproducing the bubble-nanoparticle SAXS-behavior which is known from the literature  
17  
18 [7, 13, 42].  
19  
20  
21  
22  
23  
24

25 The second reference experiment is the laser ablation of gold nanoparticles in a 0.5 mM NaCl  
26  
27 solution. The temporal distribution is given by the red circles in Figure 2b representing the  
28  
29 scattering signal from the nanoparticles. The scattering signal of nanoparticles ablated in a  
30  
31 micromolar electrolyte solution is, at almost any delay after laser impact, as low as for the  
32  
33 reference measurements at negative delays. It was shown before by means of *in situ* SAXS that  
34  
35 the size and the amount of secondary particles is reduced inside the cavitation bubble already  
36  
37 90  $\mu$ s after laser impact [7]. As XHI is mostly sensitive to secondary particles (Fig. 2a) it is  
38  
39 concluded that the size reduction decreases the scattering signal intensity below the detection  
40  
41 limit. Consequently, less to no signal is recorded.  
42  
43  
44  
45  
46

47 Just like the NaCl solution the PVP solution is prepared prior to LAL so that PVP molecules  
48  
49 are present in the liquid phase at any time during the ablation process. The blue triangles in  
50  
51 Figure 2b show the scattering signal of nanoparticles ablated in presence of PVP as a function of  
52  
53 the time delay after laser impact. Obviously, the curve progression is similar to the one in pure  
54  
55 water. The results obtained from direct measurement of the particle X-ray scattering *in situ* (i.e.  
56  
57  
58  
59  
60

1  
2  
3 inside the cavitation bubble) show that the macromolecular ligand PVP does not affect the  
4  
5 abundance of large gold nanoparticles (or aggregates) within the first 210  $\mu\text{s}$  after laser impact.  
6  
7 This result is somewhat surprising, as it has been shown by several groups that size quenching of  
8  
9 nanoparticles synthesized by LAL is possible by adding macromolecular ligands to the liquid  
10  
11 phase before performing LAL [20, 26, 59]. Still, none of the references include direct *in situ*  
12  
13 observation of the processes inside the gaseous phase of the cavitation bubble. Our data indicates  
14  
15 the ineffectiveness of macromolecular ligand functionalization during cavitation bubble  
16  
17 confinement.  
18  
19  
20  
21

22  
23 Regarding the *in situ* XHI measurements it is concluded that PVP does not act as a size  
24  
25 quenching agent for the secondary particles on the observed time scale during cavitation. This  
26  
27 might be due to slow reaction kinetics, low diffusion constant or by the partial disintegration of  
28  
29 PVP molecules by the harsh conditions induced by the laser impact. In principle, also a too low  
30  
31 concentration could cause the observed ineffectiveness of PVP. This is excluded in the following  
32  
33 section, addressing the *ex situ* analysis of size quenched nanoparticles. The size quenching  
34  
35 efficiency of micromolar solutions of NaCl has been proven before *in situ* and *ex situ*. In contrast  
36  
37 to NaCl, the macromolecular ligand PVP is less frequently used in combination with gold  
38  
39 nanoparticle for size control during LAL. It is therefore mandatory to prove the size quenching  
40  
41 ability of PVP with well-established *ex situ* methods to support the results from the *in situ* XHI.  
42  
43 As the scattering contrast of the XHI method is based on scattering of X-rays it is sensitive to  
44  
45 particle volume (mass). We will therefore compare the volume-weighted particle sizes when  
46  
47 comparing the *ex situ* to the *in situ* results. To discriminate the influence of PVP on the size of  
48  
49 the ablated gold nanoparticles, either by chemical functionality or molecular size, additional  
50  
51 ablation in N-vinylpyrrolidone (NVP), which is the monomer of PVP, was performed.  
52  
53  
54  
55  
56  
57  
58  
59  
60

The volume-weighted median diameters  $D_{50}$  of gold nanoparticle synthesized in NaCl, PVP and NVP are plotted in Figure 3a as a function of the additive-to-gold-ratio (AGR). These median diameters are derived from ADC while the ablated gold mass is calculated from the UV/Vis extinction spectra of the gold colloids. The two quantities allow for the calculation of the specific surface area. The absolute additive concentrations are varied between 1  $\mu\text{M}$  and 1,000  $\mu\text{M}$ . As shown in Figure 3a using solutions of NaCl with a concentration as low as 0.2  $\mu\text{mol}/\text{mg}$  is sufficient to start size quenching and a size reduction from 40 nm (pure water) to 12 nm in the volume-weighted average. As colloids produced in 1  $\mu\text{M}$  (0.02  $\mu\text{mol}/\text{mg}$ ) solutions of NaCl were unstable after minutes to hours independent of the AGR these results are excluded.

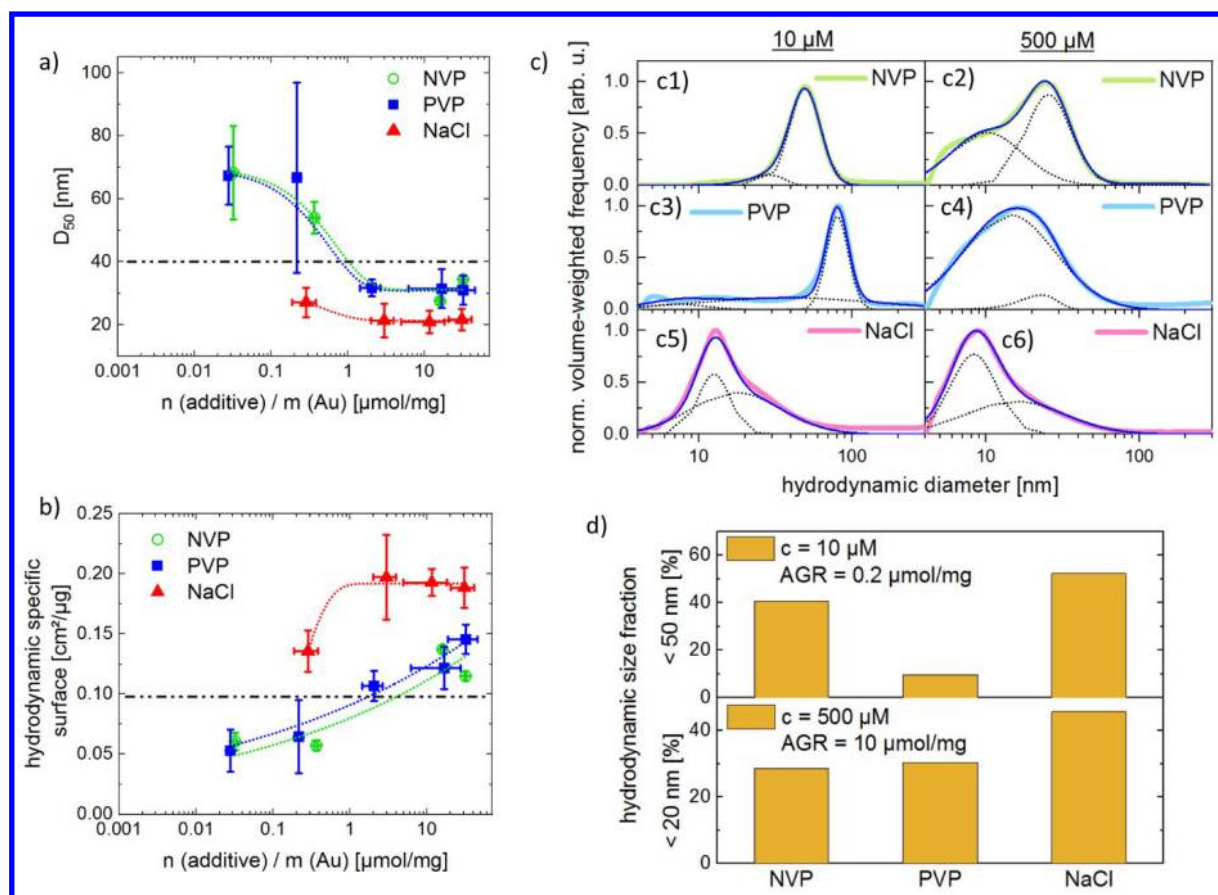


**Figure 3.** (a) Volume-weighted hydrodynamic median diameter obtained by analytical disc centrifugation and (b) related specific surface area of gold nanoparticles in PVP and NaCl as

1  
2  
3 function of the additive-to-gold ratio (AGR). The dashed-dotted horizontal lines mark the  
4  
5 reference experiments from LAL in pure water. Nanoparticle mass concentrations are obtained  
6  
7 by optical UV/Vis extinction spectroscopy. (c) Volume-weighted particle size distributions of  
8  
9 colloids in low and high additive concentrations derived from ADC analysis. (d) Hydrodynamic  
10  
11 size fractions of particles  $< 20$  nm and  $< 50$  nm. The data is derived from the ADC size  
12  
13 distributions in (c). The results display the properties of the particles in their nascent  
14  
15 hydrodynamic environment.  
16  
17  
18  
19  
20

21  
22 The function is saturated already at AGR of  $2 \mu\text{mol}/\text{mg}$  resulting in hydrodynamic nanoparticle  
23  
24 diameters of 20 nm. As these values are volume-weighted they prove the absence of considerable  
25  
26 amounts of large secondary nanoparticles or aggregates. This finding corresponds well with the  
27  
28 absence of *in situ* XHI scattering signal for NaCl in Figure 2b. PVP is suitable for size control of  
29  
30 laser generated gold nanoparticles, if high concentrations are used. Still, the trend differs  
31  
32 significantly from NaCl. While the relative concentration at saturation is similar for NaCl and  
33  
34 PVP ( $1\text{-}2 \mu\text{mol}/\text{mg}$ ) the size reducing effect is lower for PVP (minimum size only 30 nm). At  
35  
36 low concentrations ( $< 0.5 \mu\text{mol}/\text{mg}$ ) even a destabilization of particles seems to take place. The  
37  
38 specific surface dose of additives per nanoparticle surface is plotted in Figure 3b. The ordinate  
39  
40 shows the specific surface derived from ADC. The electrolyte NaCl shows a step-like behavior  
41  
42 as a function of the AGR with a saturation at  $2 \mu\text{mol}/\text{mg}$ . Regarding PVP, this plot shows that  
43  
44 the specific surface area is increasing as a function of the AGR while no saturation is reached  
45  
46 within the investigated range (Fig. 3b). In sum, the volume-weighted and surface related  
47  
48 dependencies derived from the hydrodynamic analysis indicate a size quenching efficiency that  
49  
50 is expected to correlate to the *in situ* XHI measurements (Fig. 2b) when the amount of PVP per  
51  
52  
53  
54  
55  
56  
57  
58  
59  
60

1  
2  
3 gold mass exceeds  $\sim 10 \mu\text{mol}/\text{mg}$ . Note that the absolute concentration of PVP in XHI of  $500 \mu\text{M}$   
4  
5 (equivalent to  $\sim 10 \mu\text{mol}/\text{mg}$  *ex situ*) is even higher in terms of AGR, but difficult to quantify in  
6  
7 the dynamic environment due to the unknown time-averaged ablation yield. Apart from that, an  
8  
9 effect of the PVP concentration on the laser transmission and LAL-cavitation can be excluded by  
10  
11 measuring the extinction spectrum of the pure solution and bubble dynamics (as discussed later).  
12  
13 It is concluded that PVP mainly acts as a growth quencher *ex situ* and that the effect is therefore  
14  
15 not observable *in situ*. Note that the data in Figure 3 display the hydrodynamic sizes of the  
16  
17 colloids. Keeping this in mind it is obvious that the large particles observed in PVP solutions  
18  
19 with  $\text{AGR} \leq 0.1 \mu\text{mol}/\text{mg}$  are not individual nanoparticles but rather large agglomerates (Fig.  
20  
21 S11). These are formed, just as in pure water, by insufficient repulsive forces between the  
22  
23 individual nanoparticles. While PVP binds to the gold surface the respective concentrations are  
24  
25 just too low to induce steric stabilization of the many small particles because the overall surface  
26  
27 in the system is high if the number of small particles is high as well. Therefore, the amount of  
28  
29 PVP is just enough to stabilize the reduced (total) surface of the forming agglomerates. This  
30  
31 behavior of agglomerate stabilization supports the conclusion that PVP acts as an *ex situ* growth  
32  
33 quencher rather than already *in situ* inside the cavitation bubble.  
34  
35  
36  
37  
38  
39

40 To clarify the influence of the organic ligand PVP in terms of the size of the molecules and their  
41  
42 functionality we performed additional *ex situ* experiments in different concentrations of solutions  
43  
44 of the PVP's monomer N-vinylpyrrolidone (NVP). The chemical was obtained from Acros  
45  
46 Organics (99 %, stabilized with NaOH) and used without further purification. Measurements of  
47  
48 the pH value of  $1 \mu\text{M}$  and  $1000 \mu\text{M}$  solutions of NVP revealed that it was almost unaffected,  
49  
50 with 5.9 at  $1 \mu\text{M}$  and 5.9-6.0 at  $1000 \mu\text{M}$ . Furthermore, the electrolytic conductivity was  
51  
52 constant at  $0.7\text{-}0.8 \mu\text{S}/\text{cm}$ . The volume-weighted median diameter and the specific surface area  
53  
54  
55  
56  
57  
58  
59  
60

1  
2  
3 of the gold nanoparticles was derived from combined ADC and UV/Vis analysis. The graphs in  
4  
5 the Figures 3a,b reveal an almost identical curve progression of samples produced in NVP  
6  
7 compared with those obtained in PVP but quite different to NaCl. This result points toward a  
8  
9 major influence of the additives' functionality rather than the size of the molecule. Hence, NVP  
10  
11 and PVP of the same molarity have quite similar effect on the final size of the gold nanoparticles  
12  
13 although NVP's molecular weight is only 1/35 of PVP (and roughly twice as large as that of  
14  
15 NaCl). Both organic additives, NVP and PVP, do not bear functional groups capable to  
16  
17 chemisorb on the gold surface obviously affect the size of the nanoparticles on a later time scale,  
18  
19 probably after the final collapse of the cavitation bubble.  
20  
21  
22

23  
24 The similarity of the curve progression of NVP and PVP samples in Figure 3a,b requires further  
25  
26 clarification. Therefore, in Figure 3c the size distributions (ADC, volume-weighted) of low and  
27  
28 high concentrations of NVP and PVP are compared. Additional surface-weighted size  
29  
30 distributions are presented in Figure S8. While at concentrations of 1  $\mu\text{M}$  the size distributions  
31  
32 are quite similar, at 1000  $\mu\text{M}$  the entire PVP distribution is shifted to smaller hydrodynamic  
33  
34 particle sizes whereas the NVP distribution shows only the evolution of a weaker primary mode  
35  
36 at small particle sizes. Both additives are less effective in terms of their size quenching efficiency  
37  
38 compared to NaCl (red line). The reason why the distinct differences in the size distributions of  
39  
40 NVP and PVP are not displayed in Figure 3 are that (i) the median diameter does not describe all  
41  
42 details of a size distribution and (ii) there are variations of abundance of particles larger than 100  
43  
44 nm in NVP and PVP (Fig. 3c). Accordingly, while organic ligand's the functional group seems  
45  
46 more important to size quenching compared to the molecular weight, the latter influence is not  
47  
48 negligible with regard to the hydrodynamic diameter. The reduced abundance of  
49  
50 hydrodynamically large ( $> 20$  nm) particles in PVP is a proof for steric stabilization which is  
51  
52  
53  
54  
55  
56  
57  
58  
59  
60

1  
2  
3 important for the colloid's long term stability against aggregation. This is clarified in Figure 3d  
4  
5 by plotting the relative hydrodynamic size fraction of particles  $< 50$  nm and  $< 20$  nm as a  
6  
7 function of the respective additive.  
8  
9

10 To summarize the hydrodynamic *ex situ* particle analysis, it is demonstrated that both additives  
11 result in smaller nanoparticles. Yet, while the addition of the electrolyte NaCl results in a plateau  
12 of the specific surface area already at a low AGR of  $1 \mu\text{mol}/\text{mg}$ , the macromolecular ligand does  
13 not saturate even at  $20 \mu\text{mol}/\text{mg}$ . This indicates that NaCl results in an additional energy barrier  
14 against ripening or coalescence of the nanoparticles (or their atom cluster seeds) by increasing  
15 the surface charges. On the other hand, PVP stabilizes nanoparticles sterically, building up a  
16 short-ranged steric barrier between the particles. With increasing amount of PVP molecules that  
17 barrier becomes more bulky and provides quenching of subsequent ripening processes. Hence,  
18 the hydrodynamic analysis indicates that the differing colloidal stabilizing mechanisms of NaCl  
19 and PVP also results in different size reductive effects in LAL.  
20  
21  
22  
23  
24  
25  
26  
27  
28  
29  
30  
31  
32  
33

34 To complement the *ex situ* particle analysis additional particle characterization by TEM has  
35 been performed. This is to provide additional information compared to a sole hydrodynamic  
36 analysis, as TEM is sensitive to individual nanoparticles. The results are collected in Figure 4  
37 (with TEM pictures shown in the Supporting Information, Fig. S9-S12). The left column (black  
38 bars) shows the number-weighted histograms of gold nanoparticles ablated in pure water, low  
39 ( $0.2 \mu\text{mol}/\text{mg}$ , corresponds to  $10 \mu\text{M}$ ) and high ( $10 \mu\text{mol}/\text{mg}$ , corresponds to  $500 \mu\text{M}$ ) AGRs of  
40 NaCl and PVP. It is visible that both additives reduce the size of the individual, number-  
41 weighted, nanoparticles with respect to pure water from  $19$  nm down to  $6-8$  nm with increasing  
42 AGR. As visible from the number-weighted TEM histogram in the left column of Figure 4, the  
43 nanoparticles synthesized in pure water exhibit a distinct, broad, and bimodal size distribution  
44  
45  
46  
47  
48  
49  
50  
51  
52  
53  
54  
55  
56  
57  
58  
59  
60

1  
2  
3 with an average size of 17 nm and a significant share of large solid spheres of 40-70 nm in  
4 diameter. If NaCl is used in a small AGR of 0.2  $\mu\text{mol}/\text{mg}$  the small particles (size reduction by  
5 2 nm) are less affected than the large solid spheres. The size of the latter (maximum diameter  
6 40 nm) and relative amount decrease drastically. This effect is enhanced by LAL with a high  
7 AGR of 10  $\mu\text{mol}/\text{mg}$ , which reduces the maximum size of large solid spheres to 20 nm and  
8 halves the size of the primary particles. Regarding LAL in PVP the situation is slightly different,  
9 especially at high AGR. Even an AGR of 10  $\mu\text{mol}/\text{mg}$  of PVP leaves a significant share of  
10 40 nm-particles behind. Regarding the number-weighted-histogram of gold nanoparticles in high  
11 AGR of NVP, the similarity to the size distribution in PVP is obvious. Still, the distribution is  
12 broader in NVP, while in PVP a mode at diameters as small as 6 nm is dominant which is  
13 accompanied by a shoulder in the distribution. For reasons of comparability to the *in situ* XHI  
14 analysis the histograms are also converted from number- to volume-weighted distributions. By  
15 this statistics large particles are amplified. The corresponding histograms (Fig. 4, middle column,  
16 red bars) show that NaCl indeed reduces the size and abundance of large particles, as the median  
17 diameter  $D_{50}$  is significantly reduced from 52 nm in pure water down to 10 nm at 10  $\mu\text{mol}/\text{mg}$   
18 AGR.  
19  
20  
21  
22  
23  
24  
25  
26  
27  
28  
29  
30  
31  
32  
33  
34  
35  
36  
37  
38  
39  
40  
41  
42  
43  
44  
45  
46  
47  
48  
49  
50  
51  
52  
53  
54  
55  
56  
57  
58  
59  
60

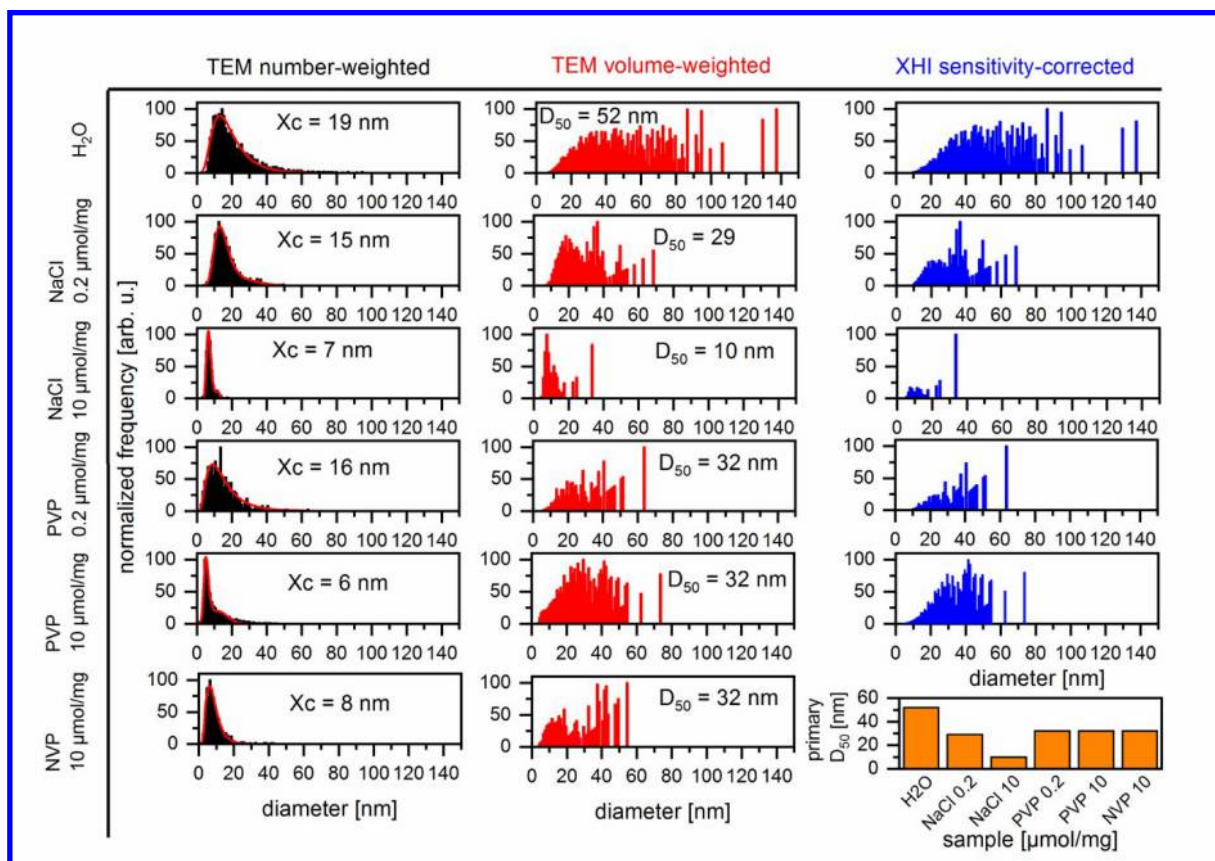


**Figure 4.** Representative TEM histograms of AuNP in pure water, NaCl and PVP at AGRs of 0.2 and 10  $\mu\text{mol/mg}$  (left column). The envelopes shown as solid red lines are obtained by lognormal fitting and the center of gravity  $X_c$  is displayed. The middle column shows the calculated volume-weighted histograms of the same samples with corresponding median diameters  $D_{50}$ . In the right column the volume-weighted histograms are further weighted by the XHI sensitivity curve shown in Figure 2a. The plot in the lower right corner sums up the volume-weighted primary particle median diameters as a function of the type and AGR of additive.

However, in the case of the macromolecule PVP the situation is different. While already small amounts of PVP (AGR of 0.2  $\mu\text{mol/mg}$ ) significantly reduce the median particle size from 52 nm to 32 nm, no further reduction in observed with increasing AGR. The volume-weighted distribution in high AGR of NVP is quite similar to that in low AGR of PVP (the lack of

1  
2  
3 particles < 60 nm is due to the low number of large particles). It is concluded that the monomer  
4 and the polymer affect the primary particles in the same way but PVP is much more effective  
5 due to its higher chain-length and the resulting improved resistance against hydrodynamic  
6 ripening of the nanoparticles. The primary median diameters (volume-weighted) are displayed in  
7 Figure 4 (lower right) as a function of additive and concentration. All used additives and  
8 concentrations reduce the median particle size by at least ~20 nm. Still, high AGRs of NaCl are  
9 the only sample that quenches the particle size even down to 10 nm, which is therefore not  
10 detectable inside the cavitation bubble by XHI.  
11  
12  
13  
14  
15  
16  
17  
18  
19  
20  
21

22 As discussed before the *in situ* XHI is sensitive to the ablated particle volume, but the overall  
23 size-dependent sensitivity is not a linear function. Therefore, the sensitivity curve (Fig. 2a) is  
24 applied to the volume-weighted TEM histograms, resulting in histograms mapped onto the XHI  
25 sensitivity shown in the right column of Figure 4 (blue bars). Significant differences in the  
26 histograms are observable as function of the liquid composition. The sensitivity-weighted  
27 histogram of the colloid produced in pure water peaks at 90 nm and exhibits an overall broad  
28 distribution. The finding fits to the *in situ* XHI analysis (Fig. 2b) as the expected strong  
29 scattering signal is indeed observed. Additionally, the high AGR of NaCl, as used for the *in situ*  
30 analysis, shows a scattering sensitivity maximum at about 35 nm, with all other particle species  
31 in the size range of  $\leq 25$  nm. Therefore, assuming that NaCl already quenches the size of  
32 nanoparticles *in situ* inside the cavitation bubble, no XHI scattering signal is expected. It is  
33 therefore plausible that the electrolyte NaCl not solely reduces aggregation inside the cavitation  
34 bubble, but also the size and abundance of individual large nanoparticles. The sensitivity-  
35 weighted TEM-histogram at 10  $\mu\text{mol}/\text{mg}$  AGR PVP peaks at 45 nm and the scattering signal  
36 remains high up to 75 nm, because of the higher sensitivity of the XHI setup towards larger  
37  
38  
39  
40  
41  
42  
43  
44  
45  
46  
47  
48  
49  
50  
51  
52  
53  
54  
55  
56  
57  
58  
59  
60

1  
2  
3 particles (Fig. 2a). Again, assuming PVP would affect the size of ablated nanoparticles already  
4  
5 inside the cavitation bubble a reduced scattering signal in XHI would result, compared to the  
6  
7 ablation in pure water. As this is not the case the conclusion is that PVP does not induce size  
8  
9 quenching to individual nanoparticles already inside the cavitation bubble, but acts as a growth  
10  
11 and ripening quencher on a later time-scale, thereby reducing the final particle size of both small  
12  
13  
14  
15 primary and large secondary particles.  
16  
17  
18  
19  
20  
21  
22  
23  
24  
25  
26  
27  
28  
29  
30  
31  
32  
33  
34  
35  
36  
37  
38  
39  
40  
41  
42  
43  
44  
45  
46  
47  
48  
49  
50  
51  
52  
53  
54  
55  
56  
57  
58  
59  
60

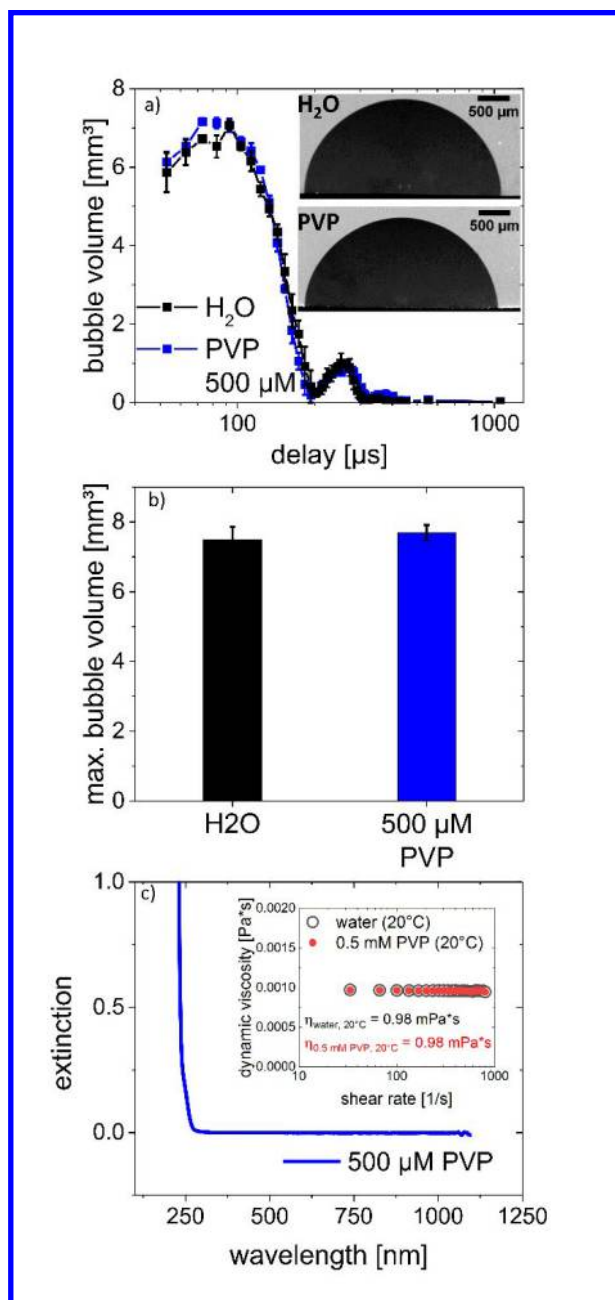


**Figure 5.** (a) Cavitation bubble dynamics as function of the delay from the laser impact. The PVP molecules do not affect the dynamics of the bubble. (b) Results of image analysis of the cavitation bubble at its maximum extension at 93 μs after laser impact on the target showing no difference between pure water and 500 μM PVP solution. (c) UV/Vis extinction spectrum of a 500 μM PVP solution. The solution is transparent at the laser wavelength of 1064 nm. Inset: Dynamic viscosity of pure water and a 0.5 mM PVP solution.

1  
2  
3  
4  
5  
6 As both the *in situ* and the *ex situ* (hydrodynamic and structural analysis) point towards a  
7  
8 growth quenching mechanism of the macromolecular ligand PVP at a time-scale after the  
9  
10 lifetime of the cavitation bubble, we need to exclude processes related to the laser ablation and  
11  
12 cavitation itself that might cause this behavior. For example, Tsuji et al. have found a size  
13  
14 quenching effect of PVP on silver nanoparticles during LAL [29]. They attributed this effect at  
15  
16 least partially to the reduced size and lifetime of the laser-induced cavitation bubble, when PVP  
17  
18 was used instead of pure water. Still, in our case the situation is different. The molecular weight  
19  
20 of the PVP used in the present study is almost three times lower compared to Tsuji et al. [29],  
21  
22 additionally the concentration we used for the *in situ* analysis (500  $\mu\text{M}$ ) is 36 times lower here .  
23  
24 Overall this sums up to a negligible (factor of 108) influence of the PVP on the hydrodynamics.  
25  
26 This is verified by performing shadowgraphic imaging of the cavitation bubble produced during  
27  
28 LAL of gold in water with 500  $\mu\text{M}$  PVP. As shown in Figure 5b the maximum bubble volume  
29  
30 (93  $\mu\text{s}$  after laser impact) is independent of the presence of PVP molecules. Therefore, it is  
31  
32 underlined that the effective laser fluence on the gold target surface is the same for both liquids,  
33  
34 as it is known that the cavitation bubble volume scales with the laser fluence [19]. The overall  
35  
36 dynamics of the cavitation bubble (e.g. the volume and peak time of the bubble rebound) are also  
37  
38 not significantly affected by the PVP molecules as shown in Figure 5a. The effective laser  
39  
40 fluence on the target surface due to absorption in the solution is not expected to be affected by  
41  
42 the low concentration of the used PVP (3,500 g/mol). The UV/Vis extinction spectrum of the  
43  
44 pure PVP solution is given in Figure 5c, with the measured viscosity of water and the PVP  
45  
46 solution given in the inset. Obviously, there is no measurable extinction at the laser wavelength  
47  
48 of 1064 nm.  
49  
50  
51  
52  
53  
54  
55  
56  
57  
58  
59  
60

## CONCLUSIONS

Improvement of size dispersion of laser-generated colloids is often achieved *in situ* by anion-based charge transfer or organic ligands with high-affinity functional groups. Less is known about the quenching mechanism of macromolecular ligands, in particular non-thiolated polymers. To differentiate between the mechanisms of nanoparticle growth quenching by anions and macromolecules, we performed *in situ* X-ray multi-contrast imaging (with scattering contrast from a Hartmann mask) during pulsed laser ablation in liquids of gold combined with thorough *ex situ* evaluation. By using pure water and micromolar solutions of NaCl and PVP we have shown, that while NaCl reduces the size of primary and secondary nanoparticles already inside the gas phase of the laser-induced cavitation bubble, PVP does not change the nanoparticle size with respect to the sizes found in pure water. The maximum of size sensitivity in XHI is at 55 nm, which allows for the conclusion that the organic ligand PVP does not significantly alter the size of secondary nanoparticles, composed of large solid spheres and aggregates, inside the cavitation bubble. By studying the influences of the electrolyte NaCl and the macromolecular ligand PVP on the size and size distributions obtained *ex situ*, i.e., after final collapse of the cavitation bubble, it is found that PVP does reduce the size of small primary nanoparticles ( $d < 10$  nm) and also the degree of aggregation. In general, the concentration of PVP must exceed a threshold to effectively reduce the size of aggregates compared to pure water. The used concentration of 0.5 mM is well above that threshold. One major difference between the additives NaCl and PVP is their impact on large secondary spheres. The combined results point towards the conclusion that PVP interacts with nanoparticles produced by LAL by a different mechanism as NaCl (as large particle size quenching is not observed). It is also indicated that

1  
2  
3 primary and secondary particles are formed by different ablation mechanisms as large spheres  
4  
5 can be affected by PVP *ex situ* more efficiently than small particles, possibly via coalescence  
6  
7 quenching in colloidal state.  
8  
9

## 10 11 12 ASSOCIATED CONTENT 13

### 14 15 **Supporting Information**

16  
17 The following file is available free of charge.

18  
19  
20 Influence of the effective laser fluence on the nanoparticle size distribution (Fig. S1); UV/vis  
21  
22 calibration graph for determination of gold concentrations and representative UV/Vis extinction  
23  
24 spectra (Fig. S2); schema of the setup for shadowgraphic imaging (Fig. S3); image sequences  
25  
26 highlighting the maximum extension (Fig. S4) and the evolution of the cavitation bubble in pure  
27  
28 water and in PVP solution (Fig. S5-S6); *in situ* SAXS-histogram of gold nanoparticles in water  
29  
30 and salt solution (Fig. S7); surface-weighted hydrodynamic size distributions of gold in NVP,  
31  
32 PVP, and NaCl (Fig. S8), TEM images of gold nanoparticle obtained in pure water, NaCl, PVP,  
33  
34 and NVP solutions (Fig. S9-S12). (PDF)  
35  
36  
37  
38  
39  
40  
41

## 42 43 44 AUTHOR INFORMATION

### 45 46 **Corresponding Author**

47  
48 \*e-mail: bilal.goekce@uni-due.de

49  
50  
51 \*anton.plech@kit.edu

### 52 53 54 **Author Contributions**

1  
2  
3 Alexander Letzel, Stefan Reich, and Anton Plech conducted the *in situ* experiments at the ESRF  
4 synchrotron. Stefan Reich and Anton Plech performed data acquisition and interpretation. Stefan  
5 Reich performed deconvolution of the different contrast from XHI. Alexander Rack and Margie  
6 Olbinado were the local ESRF contact persons and assisted in local setup and data handling.  
7  
8 Tomy dos Santos Rolo contributed in the planning phase and further discussions after *in situ* data  
9 acquisition. Alexander Kanitz and Jan Hoppius produced the Hartmann mask under the  
10 supervision of Andreas Ostendorf. The *ex situ* experiments and data interpretation were done by  
11 Alexander Letzel. Stephan Barcikowski, Bilal Gökce, and Anton Plech are responsible for the  
12 general conception and design of the study.  
13  
14  
15  
16  
17  
18  
19  
20  
21  
22  
23  
24

25 All authors have read and given approval to the final version of the manuscript.  
26  
27

28 ‡The authors Alexander Letzel and Stefan Reich contributed equally.  
29  
30

### 31 **Funding Sources**

32  
33

34 German Research Foundation DFG (BA3580/15-2 and PL325/8-2). Helmholtz Association  
35 within the program “Structure: From matter to materials and life”.  
36  
37  
38

### 39 **ACKNOWLEDGMENT**

40

41 Funding by the German Research Foundation DFG (BA3580/15-2 and PL325/8-2) and the  
42 Helmholtz Association within the program “Structure: From matter to materials and life” is  
43 gratefully acknowledged. We also thank the ESRF (Grenoble, France) and KARA (Karlsruhe,  
44 Germany) for providing the beam time, the latter for test measurements. We would further like to  
45 thank Jurij Jakobi for execution of the transmission electron microscopy analysis.  
46  
47  
48  
49  
50  
51  
52  
53

### 54 **ABBREVIATIONS**

55  
56  
57  
58  
59  
60

1  
2  
3 AGR, additive-to-gold ratio; LAL, laser ablation in liquids; NVP: N-vinylpyrrolidone; PVP,  
4 polyvinylpyrrolidone; XHI, X-ray Hartmann mask imaging  
5  
6  
7  
8  
9  
10

11 REFERENCES  
12

13  
14  
15 [1] A. Fojtik, A. Henglein, *Laser Ablation of Films and Suspended Particles in a Solvent:*  
16 *Formation of Cluster and Colloid Solution*, Ber. Bunsenges. Phys. Chem. 97 (1993) 252-254.  
17

18 [2] D. Zhang, B. Gökce, S. Barcikowski, *Laser Synthesis and Processing of Colloids:*  
19 *Fundamentals and Applications*, Chem. Rev. 117 (2017) 3990-4103.  
20  
21

22 [3] V. Merk, C. Rehbock, F. Becker, U. Hagemann, H. Nienhaus, S. Barcikowski, *In Situ*  
23 *Non-DLVO Stabilization of Surfactant-Free, Plasmonic Gold Nanoparticles: Effect of*  
24 *Hofmeister's Anions*, Langmuir 30 (2014) 4213-4222.  
25  
26  
27  
28

29 [4] C. Rehbock, V. Merk, L. Gamrad, R. Streubel, S. Barcikowski, *Size control of laser-*  
30 *fabricated surfactant-free gold nanoparticles with highly diluted electrolytes and their*  
31 *subsequent bioconjugation*, Phys. Chem. Chem. Phys. 15 (2013) 3057-3067.  
32  
33  
34  
35

36 [5] G. Marzun, J. Nakamura, X. Zhang, S. Barcikowski, P. Wagener, *Size control and*  
37 *supporting of palladium nanoparticles made by laser ablation in saline solution as a facile route*  
38 *to heterogeneous catalysts*, Appl. Surf. Sci. 348 (2015) 75-84.  
39  
40  
41  
42

43 [6] M. Fischer, J. Hormes, G. Marzun, P. Wagener, U. Hagemann, S. Barcikowski, *In Situ*  
44 *Investigations of Laser-Generated Ligand-Free Platinum Nanoparticles by X-ray Absorption*  
45 *Spectroscopy: How Does the Immediate Environment Influence the Particle Surface?*, Langmuir  
46  
47  
48  
49  
50  
51  
52  
53  
54  
55  
56  
57  
58  
59  
60

- 1  
2  
3 [7] A. Letzel, B. Gökce, P. Wagener, S. Ibrahimkutty, A. Menzel, A. Plech, S. Barcikowski,  
4 *Size Quenching during Laser Synthesis of Colloids Happens Already in the Vapor Phase of the*  
5 *Cavitation Bubble*, J. Phys. Chem. C 121 (2017) 5356-5365.  
6  
7  
8  
9  
10 [8] T. Tsuji, Y. Tsuboi, N. Kitamura, M. Tsuji, *Microsecond-resolved imaging of laser*  
11 *ablation at solid–liquid interface: investigation of formation process of nano-size metal colloids*,  
12 *Appl. Surf. Sci.* 229 (2004) 365-371.  
13  
14  
15  
16  
17 [9] R. Tanabe, T.T.P. Nguyen, T. Sugiura, Y. Ito, *Bubble dynamics in metal nanoparticle*  
18 *formation by laser ablation in liquid studied through high-speed laser stroboscopic videography*,  
19 *Appl. Surf. Sci.* 351 (2015) 327-331.  
20  
21  
22  
23  
24 [10] J. Lam, J. Lombard, C. Dujardin, G. Ledoux, S. Merabia, D. Amans, *Dynamical study of*  
25 *bubble expansion following laser ablation in liquids*, *Appl. Phys. Lett.* 108 (2016) 074104.  
26  
27  
28  
29 [11] A. De Giacomo, M. Dell'Aglio, F. Colao, R. Fantoni, *Double pulse laser produced*  
30 *plasma on metallic target in seawater: basic aspects and analytical approach*, *Spectrochimica*  
31 *Acta Part B: Atomic Spectroscopy* 59 (2004) 1431-1438.  
32  
33  
34  
35 [12] A. Matsumoto, A. Tamura, T. Honda, T. Hirota, K. Kobayashi, S. Katakura, N. Nishi, K.-  
36 i. Amano, K. Fukami, T. Sakka, *Transfer of the Species Dissolved in a Liquid into Laser*  
37 *Ablation Plasma: An Approach Using Emission Spectroscopy*, J. Phys. Chem. C 119 (2015)  
38 26506-26511.  
39  
40  
41  
42  
43  
44 [13] S. Ibrahimkutty, P. Wagener, A. Menzel, A. Plech, S. Barcikowski, *Nanoparticle*  
45 *formation in a cavitation bubble after pulsed laser ablation in liquid studied with high time*  
46 *resolution small angle x-ray scattering*, *Appl. Phys. Lett.* 101 (2012) 103104.  
47  
48  
49  
50  
51 [14] M.R. Gavrilović, *Impact of the cavitation bubble on a plasma emission following laser*  
52 *ablation in liquid*, *Eur. Phys. J. D* 71 (2017) 316.  
53  
54  
55  
56  
57  
58  
59  
60

- 1  
2  
3 [15] A. Tamura, T. Sakka, K. Fukami, Y.H. Ogata, *Dynamics of cavitation bubbles generated*  
4 *by multi-pulse laser irradiation of a solid target in water*, Appl. Phys. A 112 (2013) 209-213.  
5  
6  
7 [16] T. dos Santos Rolo, S. Reich, D. Karpov, S. Gasilov, D. Kunka, E. Fohtung, T.  
8  
9 Baumbach, A. Plech, *A Shack-Hartmann Sensor for Single-Shot Multi-Contrast Imaging with*  
10 *Hard X-rays*, Applied Sciences 8 (2018) 737.  
11  
12  
13 [17] S. Reich, J. Göttlicher, A. Letzel, B. Gökce, S. Barcikowski, T. dos Santos Rolo, T.  
14  
15 Baumbach, A. Plech, *X-ray spectroscopic and stroboscopic analysis of pulsed laser ablation of*  
16 *Zn and its oxidation*, Appl. Phys. A 124 (2018) 71.  
17  
18  
19 [18] S. Ibrahimkutty, P. Wagener, T. dos Santos Rolo, D. Karpov, A. Menzel, T. Baumbach,  
20  
21 S. Barcikowski, A. Plech, *A hierarchical view on material formation during pulsed-laser*  
22 *synthesis of nanoparticles in liquid*, Sci. Rep. (2015) 5:16313.  
23  
24  
25 [19] S. Reich, P. Schönfeld, A. Letzel, S. Kohsakowski, M. Olbinado, B. Gökce, S.  
26  
27 Baumbach, A. Plech, *Fluence Threshold Behaviour on Ablation and Bubble Formation in*  
28 *Pulsed Laser Ablation in Liquids*, ChemPhysChem 18 (2017) 1084-1090.  
29  
30  
31 [20] S. Besner, A.V. Kabashin, F.M. Winnik, M. Meunier, *Synthesis of Size-Tunable Polymer-*  
32 *Protected Gold Nanoparticles by Femtosecond Laser-Based Ablation and Seed Growth*, The  
33 *Journal of Physical Chemistry C* 113 (2009) 9526-9531.  
34  
35  
36 [21] R. Zamiri, B.Z. Azmi, M. Darroudi, A.R. Sadrolhosseini, M.S. Husin, A.W. Zaidan,  
37  
38 M.A. Mahdi, *Preparation of starch stabilized silver nanoparticles with spatial self-phase*  
39 *modulation properties by laser ablation technique*, Applied Physics A 102 (2011) 189-194.  
40  
41  
42 [22] F. Spano, A. Massaro, L. Blasi, M. Malerba, R. Cingolani, A. Athanassiou, *In Situ*  
43 *Formation and Size Control of Gold Nanoparticles into Chitosan for Nanocomposite Surfaces*  
44 *with Tailored Wettability*, Langmuir 28 (2012) 3911-3917.  
45  
46  
47  
48  
49  
50  
51  
52  
53  
54  
55  
56  
57  
58  
59  
60

- 1  
2  
3 [23] S. Petersen, J. Jakobi, S. Barcikowski, *In situ bioconjugation - Novel laser based*  
4 *approach to pure nanoparticleconjugates*, Appl. Surf. Sci. 255 (2009) 5435-5438.  
5  
6  
7 [24] H. Usui, Y. Shimizu, T. Sasaki, N. Koshizaki, *Photoluminescence of ZnO Nanoparticles*  
8 *Prepared by Laser Ablation in Different Surfactant Solutions*, The Journal of Physical Chemistry  
9 B 109 (2005) 120-124.  
10  
11  
12 [25] S. Salmaso, P. Caliceti, V. Amendola, M. Meneghetti, J.P. Magnusson, G. Pasparakis, C.  
13 Alexander, *Cell up-take control of gold nanoparticles functionalized with a thermoresponsive*  
14 *polymer*, J. Mater. Chem. 19 (2009) 1608-1615.  
15  
16  
17 [26] J. Tomko, J.J. Naddeo, R. Jimenez, Y. Tan, M. Steiner, J.M. Fitz-Gerald, D.M. Bubb,  
18 S.M. O'Malley, *Size and polydispersity trends found in gold nanoparticles synthesized by laser*  
19 *ablation in liquids*, Phys. Chem. Chem. Phys. 17 (2015) 16327-16333.  
20  
21  
22 [27] D. Amans, C. Malaterre, M. Diouf, C. Mancini, F. Chaput, G. Ledoux, G. Breton, Y.  
23 Guillin, C. Dujardin, K. Masenelli-Varlot, P. Perriat, *Synthesis of Oxide Nanoparticles by Pulsed*  
24 *Laser Ablation in Liquids Containing a Complexing Molecule: Impact on Size Distributions and*  
25 *Prepared Phases*, J. Phys. Chem. C 115 (2011) 5131-5139.  
26  
27  
28 [28] R. Singh, R.K. Soni, *Laser synthesis of aluminium nanoparticles in biocompatible*  
29 *polymer solutions*, Applied Physics A 116 (2014) 689-701.  
30  
31  
32 [29] T. Tsuji, D.-H. Thang, Y. Okazaki, M. Nakanishi, Y. Tsuboi, M. Tsuji, *Preparation of*  
33 *silver nanoparticles by laser ablation in polyvinylpyrrolidone solutions*, Appl. Surf. Sci. 254  
34 (2008) 5224-5230.  
35  
36  
37 [30] X. Liu, F. Zhnag, R. Huang, C. Pan, J. Zhu, *Capping Modes in PVP-Directed Silver*  
38 *Nanocrystal Growth: Multi-Twinned Nanorods versus Single-Crystalline Nano-Hexapods*, Cryst.  
39 Growth Des. 8 (2008) 1916-1923.  
40  
41  
42  
43  
44  
45  
46  
47  
48  
49  
50  
51  
52  
53  
54  
55  
56  
57  
58  
59  
60

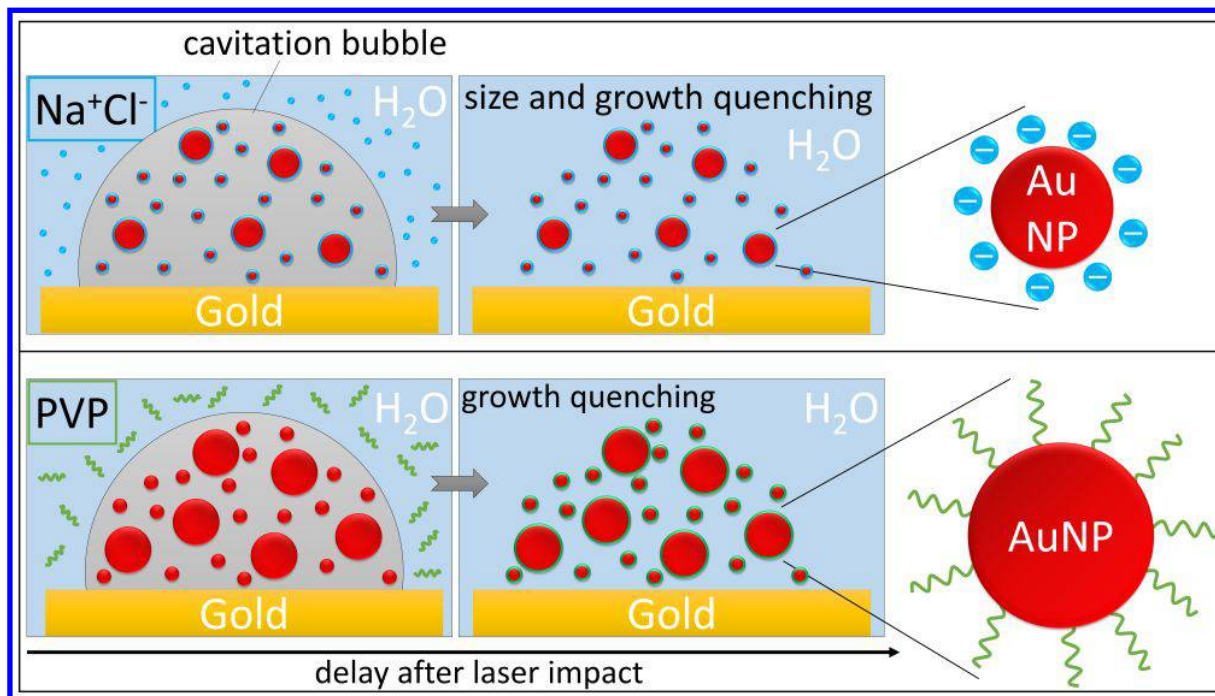
- 1  
2  
3 [31] A. Mezni, T. Dammak, A. Fkiri, A. Mlayah, Y. Abid, L.S. Smiri, *Photochemistry at the*  
4 *Surface of Gold Nanoprisms from Surface-Enhanced Raman Scattering Blinking*, J. Phys. Chem.  
5  
6 C 118 (2014) 17956-17967.  
7  
8  
9  
10 [32] L. Xu, G. Wang, X. Zheng, H. Pan, J. Zhu, Z. Li, S.-H. Yu, *Competitive Adsorption*  
11 *between a Polymer and Its Monomeric Analog Enables Precise Modulation of Nanowire*  
12 *Synthesis*, Chem 4 (2018) 2451-2462.  
13  
14  
15  
16 [33] R. Seoudi, A.A. Fouda, Elmenshawy, *Synthesis, characterization and vibrational*  
17 *spectroscopic studies of different particle size of gold nanoparticle capped with*  
18 *polyvinylpyrrolidone*, Physica B 405 (2010) 906-911.  
19  
20  
21  
22  
23 [34] H.L. Liu, P. Hou, *Low-temperature synthesis and characterization of PVP-capped FeAu*  
24 *nanoparticles*, J. Mater. Res. 26 (2011) 2040-2049.  
25  
26  
27  
28 [35] P. Abdulkin, T.L. Precht, B.R. Knappett, H.E. Skelton, D.A. Jefferson, A.E.H. Wheatley,  
29 *Systematic Control of Size and Morphology in the Synthesis of Gold Nanoparticles*, Part. Part.  
30 *Syst. Chem.* 31 (2014) 571-579.  
31  
32  
33  
34 [36] D.P. Stankus, S.E. Lohse, J.E. Hutchison, J.A. Nason, *Interactions between Natural*  
35 *Organic Matter and Gold Nanoparticles Stabilized with Different Organic Capping Agents*,  
36 *Environ. Sci. Technol.* 45 (2011) 3238-3244.  
37  
38  
39  
40 [37] K.I. Requejo, A.V. Liopo, P.J. Derry, E.R. Zubarev, *Accelerating Gold Nanorod*  
41 *Synthesis with Nanomolar Concentrations of Poly(vinylpyrrolidone)*, Langmuir 33 (2017)  
42 12681-12688.  
43  
44  
45  
46 [38] T. Tsuji, M. Nakanishi, T. Mizuki, S. Ozono, M. Tsuji, Y. Tsuboi, *Preparation and*  
47 *Shape-Modification of Silver Colloids by Laser Ablation in Liquids: A Brief Review*, Sci. Adv.  
48 *Mater.* 4 (2012) 391-400.  
49  
50  
51  
52  
53  
54  
55  
56  
57  
58  
59  
60

- 1  
2  
3 [39] C.L. Sajti, S. Petersen, A. Menéndez-Manjón, S. Barcikowski, *In-situ bioconjugation in*  
4 *stationary media and in liquid flow by femtosecond laser ablation*, Appl. Phys. A 101 (2010)  
5 259-264.  
6  
7  
8  
9  
10 [40] C.L. Sajti, A. Barchanski, P. Wagener, S. Klein, S. Barcikowski, J. Phys. Chem. C 115  
11 (2011) 5094-5101.  
12  
13  
14 [41] S. Jendrzej, B. Gökce, V. Amendola, S. Barcikowski, *Barrierless growth of precursor-*  
15 *free, ultrafast laser-fragmented noble metal nanoparticles by colloidal atom clusters - A kinetic*  
16 *in situ study*, J. Colloid. Interface Sci. 463 (2016) 299-307.  
17  
18  
19  
20  
21 [42] P. Wagener, S. Ibrahimkuty, A. Menzel, A. Plech, S. Barcikowski, *Dynamics of silver*  
22 *nanoparticle formation and agglomeration inside the cavitation bubble after pulsed laser*  
23 *ablation in liquid*, Phys. Chem. Chem. Phys. 15 (2013) 3068-3074.  
24  
25  
26  
27  
28 [43] H.H. Wen, E.E. Bennett, M.M. Hedegus, S.C. Carroll, *Spatial Harmonic Imaging of X-*  
29 *ray Scattering—Initial Results*, IEEE T. Med. Imaging 27 (2008) 997-1002.  
30  
31  
32  
33 [44] Y. Liu, B. Ahr, A. Linkin, G.J. Diebold, C. Rose-Petruck, *X-ray spatial harmonic*  
34 *imaging of phase objects*, Opt. Lett. 36 (2011) 2209-2211.  
35  
36  
37  
38 [45] S.K. Lynch, V. Pai, J. Auxier, A.F. Stein, E.E. Bennett, C.K. Kamble, X. Xiao, W.-K.  
39 Lee, N.Y. Morgan, H.H. Wen, *Interpretation of dark-field contrast and particle-size selectivity*  
40 *in grating interferometers*, Appl. Opt. 50 (2011) 4310-4319.  
41  
42  
43  
44 [46] A.F. Stein, J. Ilavsky, R. Kopace, E.E. Bennett, H. Wen, *Selective imaging of nano-*  
45 *particle contrast agents by a single-shot x-ray diffraction technique*, Opt. Express 18 (2010)  
46 13271-13278.  
47  
48  
49  
50  
51  
52  
53  
54  
55  
56  
57  
58  
59  
60

- 1  
2  
3 [47] F.A. Vittoria, M. Endrizzi, P.C. Diemoz, A. Zamir, U.H. Wagner, C. Rau, I.K. Robinson,  
4 A. Olivio, *X-ray absorption, phase and dark-field tomography through a beam tracking*  
5 *approach*, Sci. Rep. 5 (2015) 16318.  
6  
7  
8  
9  
10 [48] G.M. Hale, M.R. Querry, *Optical Constants of Water in the 200-nm to 200- $\mu$ m*  
11 *Wavelength Region*, Applied Optics 12 (1973) 555-563.  
12  
13  
14 [49] T. Wagner, *thorstenwagner/ij-particlesizer: ParticleSizer 1.0.7*, in,  
15 <https://zenodo.org/record/163568#.WoqZWXwiFpg>, 2016.  
16  
17  
18  
19 [50] H.H. Wen, E.E. Bennett, R. Kopace, A.F. Stein, V. Pai, *Single-shot x-ray differential*  
20 *phase-contrast and diffraction imaging using two-dimensional transmission gratings*, Opt. Lett.  
21 35 (2010) 1932-1934.  
22  
23  
24  
25  
26 [51] S. Reich, T. dos Santos Rolo, A. Letzel, T. Baumbach, A. Plech, *Scalable, large area*  
27 *compound array refractive lens for hard X-rays*, Applied Physics Letters 112 (2018) 151903.  
28  
29  
30 [52] S. Kaeppeler, F. Bayer, T. Weber, A. Maier, G. Anton, J. Hornegger, M. Beckmann, P.A.  
31 Fasching, A. Hartmann, F. Heindl, T. Michel, G. Oezguel, G. Pelzer, C. Rauh, J. Rieger, R.  
32 Schulz-Wendtland, M. Uder, D. Wachter, E. Wenkel, C. Riess, *Signal decomposition for X-ray*  
33 *dark-field imaging*, Med. Image. Comput. Comput. Assist. Interv. 17 (2014) 170-177.  
34  
35  
36  
37  
38 [53] G.-R. Zhang, B.-Q. Xu, *Surprisingly strong effect of stabilizer on the properties of Au*  
39 *nanoparticles and Pt<sup>+</sup>Au nanostructures in electrocatalysis*, Nanoscale 2 (2010) 2798-2804.  
40  
41  
42  
43  
44 [54] H. Tsunoyama, N. Ichikuni, H. Sakurai, T. Tsukuda, *Effect of Electronic Structures of Au*  
45 *Clusters Stabilized by Poly(N-vinyl-2-pyrrolidone) on Aerobic Oxidation Catalysis*, Journal of  
46 the American Chemical Society 131 (2009) 7086-7093.  
47  
48  
49  
50  
51  
52  
53  
54  
55  
56  
57  
58  
59  
60

- 1  
2  
3 [55] M. Okumura, Y. Kitagawa, T. Kawakami, M. Haruta, *Theoretical investigation of the*  
4 *hetero-junction effect in PVP-stabilized Au13 clusters. The role of PVP in their catalytic*  
5 *activities*, Chemical Physics Letters 459 (2008) 133-136.  
6  
7  
8  
9  
10 [56] H. Wang, X. Qiao, J. Chen, X. Wang, S. Ding, *Mechanisms of PVP in the preparation of*  
11 *silver nanoparticles*, Mater. Chem. Phys. 94 (2005) 449-453.  
12  
13  
14 [57] F. Pfeiffer, M. Bech, O. Bunk, P. Kraft, E.F. Eikenberry, C. Brönnimann, C. Grünzweig,  
15 C. David, *Hard-X-ray dark-field imaging using a grating interferometer*, Nat. Mater. 7 (2008)  
16 134-137.  
17  
18  
19  
20  
21 [58] A. Letzel, B. Gökce, A. Menzel, A. Plech, S. Barcikowski, *Primary particle diameter*  
22 *differentiation and bimodality identification by five analytical methods using gold nanoparticle*  
23 *size distributions synthesized by pulsed laser ablation in liquids*, Appl. Surf. Sci. 435 (2018) 743-  
24 751.  
25  
26  
27  
28  
29  
30  
31 [59] P. Wagener, G. Brandes, A. Schwenke, S. Barcikowski, *Impact of in situ polymer coating*  
32 *on particle dispersion into solid laser-generated nanocomposites*, Physical Chemistry Chemical  
33 Physics 13 (2011) 5120-5126.  
34  
35  
36  
37  
38  
39  
40  
41  
42  
43  
44  
45  
46  
47  
48  
49  
50  
51  
52  
53  
54  
55  
56  
57  
58  
59  
60

## TABLE OF CONTENTS



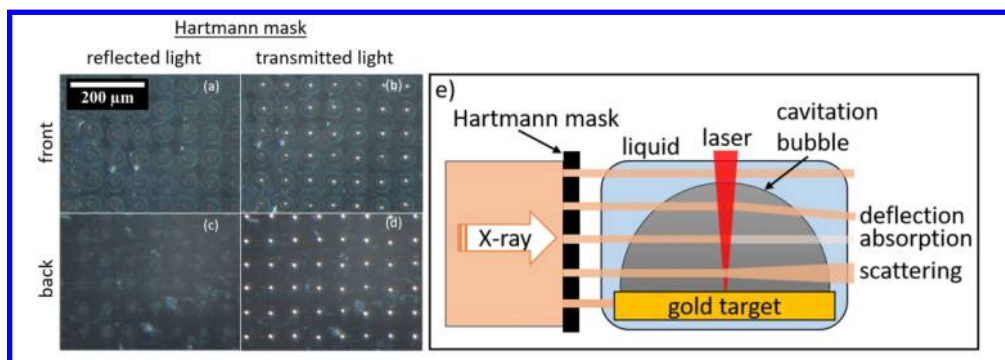


Figure 1. Images of the Pt foil acting as a Hartmann mask for in situ experiments obtained by optical microscopy. Front of the mask in reflected (a) and transmitted light mode (b). The laser-drilled holes are funnel-shaped on the front side (side at which the laser beam impinges). Back of the mask in reflected (c) and transmitted light mode (d). Sketch of the XHI approach with the incoming X-ray beam being split into multiple beamlets by the Hartmann mask, and undergoing absorption, differential phase shift (deflection) and diffuse scattering (broadening) when crossing the cavitation bubble and the confined nanoparticles (e).

160x54mm (300 x 300 DPI)

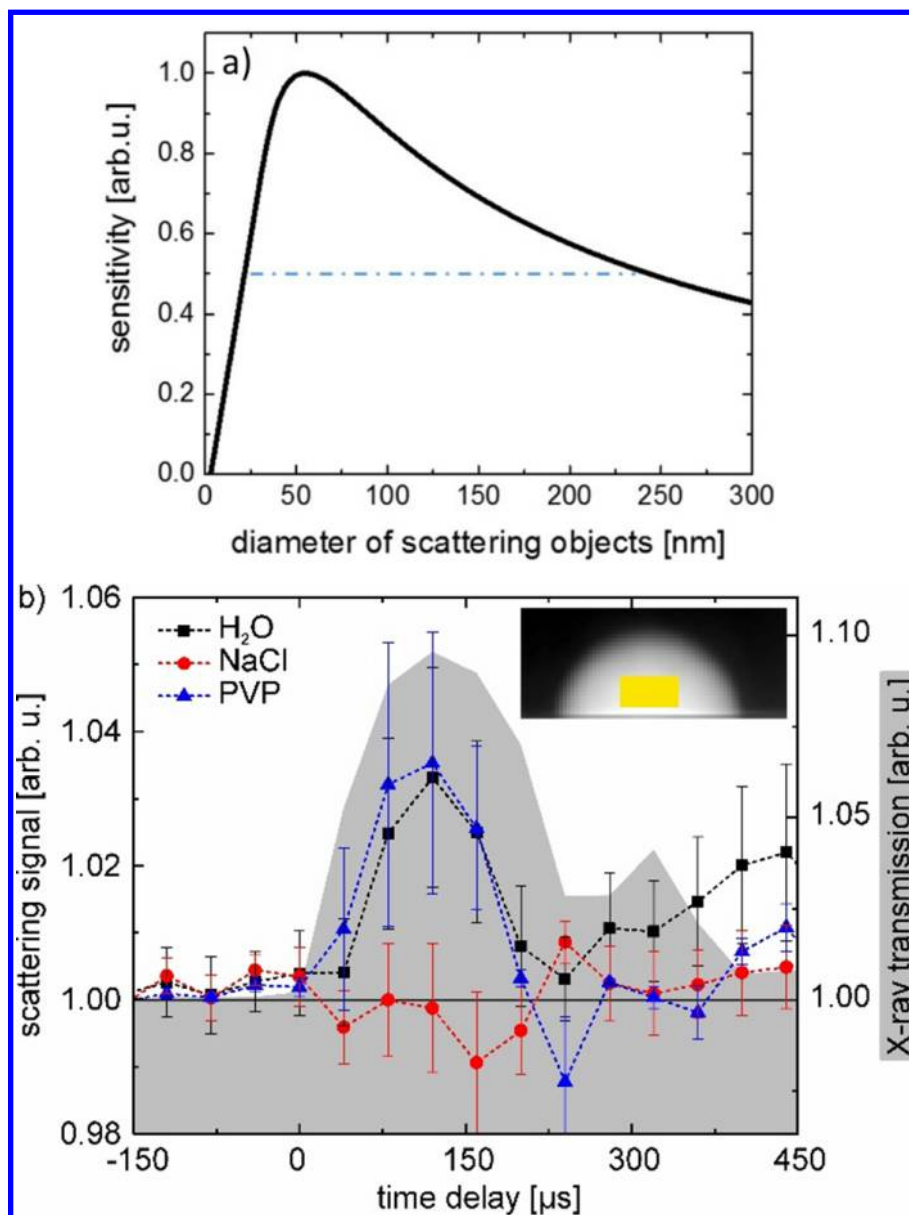


Figure 2. Scattering sensitivity on nanoparticles as function of the scattering object size for the given setup. The blue dashed-dotted line indicates the size interval above 50 % relative sensitivity (a). Scattering signal as function of the delay after laser impact obtained at the center of the cavitation bubble (inset shows the transmission signal together with the region of interest) (b). Scattering signals of gold nanoparticles in pure water (black squares), NaCl- (red circles) and PVP-solution (blue triangle) (both 0.5 mM). The shaded curve represents the change in X-ray transmission starting from 1 (0 % intensity change) before laser arrival. Error bars are the standard deviation between several runs.

80x106mm (300 x 300 DPI)

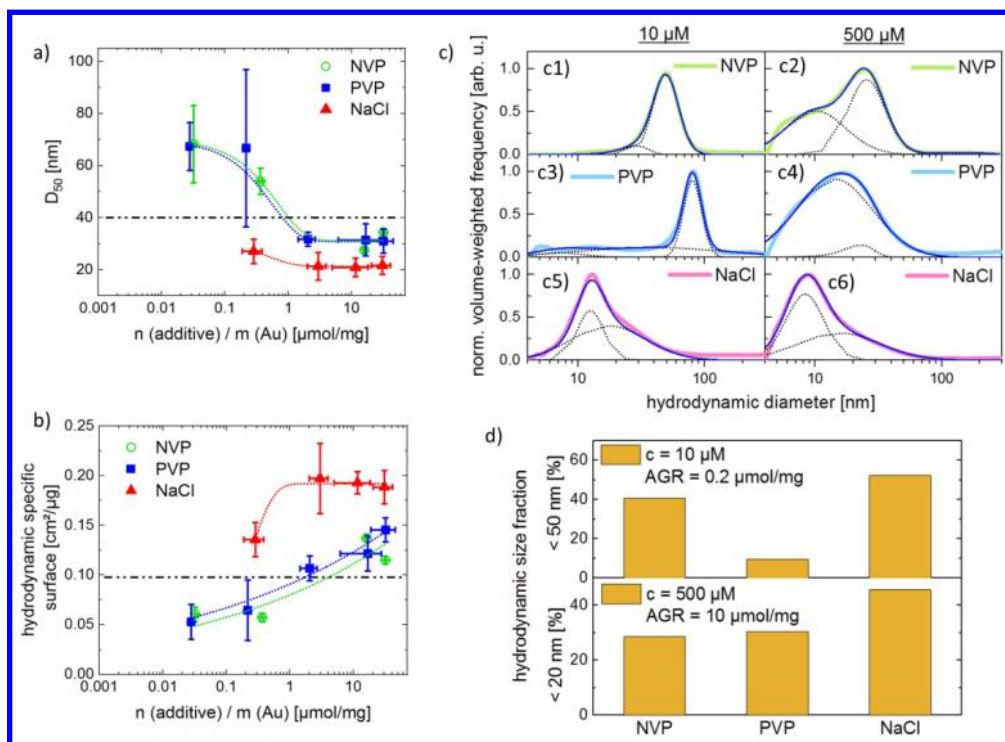


Figure 3. (a) Volume-weighted hydrodynamic median diameter obtained by analytical disc centrifugation and (b) related specific surface area of gold nanoparticles in PVP and NaCl as function of the additive-to-gold ratio (AGR). The dashed-dotted horizontal lines mark the reference experiments from LAL in pure water. Nanoparticle mass concentrations are obtained by optical UV/Vis extinction spectroscopy. (c) Volume-weighted particle size distributions of colloids in low and high additive concentrations derived from ADC analysis. (d) Hydrodynamic size fractions of particles < 20 nm and < 50 nm. The data is derived from the ADC size distributions in (c). The results display the properties of the particles in their nascent hydrodynamic environment.

160x115mm (300 x 300 DPI)

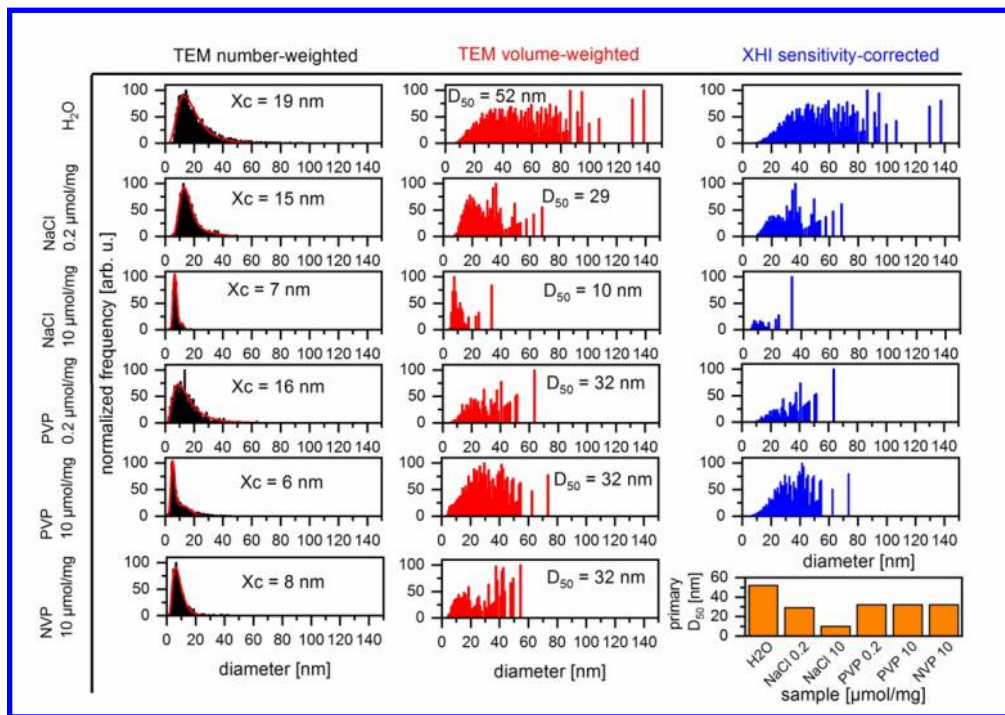


Figure 4. Representative TEM histograms of AuNP in pure water, NaCl and PVP at AGRs of 0.2 and 10  $\mu\text{mol}/\text{mg}$  (left column). The envelopes shown as solid red lines are obtained by lognormal fitting and the center of gravity  $X_c$  is displayed. The middle column shows the calculated volume-weighted histograms of the same samples with corresponding median diameters  $D_{50}$ . In the right column the volume-weighted histograms are further weighted by the XHI sensitivity curve shown in Figure 2a. The plot in the lower right corner sums up the volume-weighted primary particle median diameters as a function of the type and AGR of additive.

160x111mm (300 x 300 DPI)

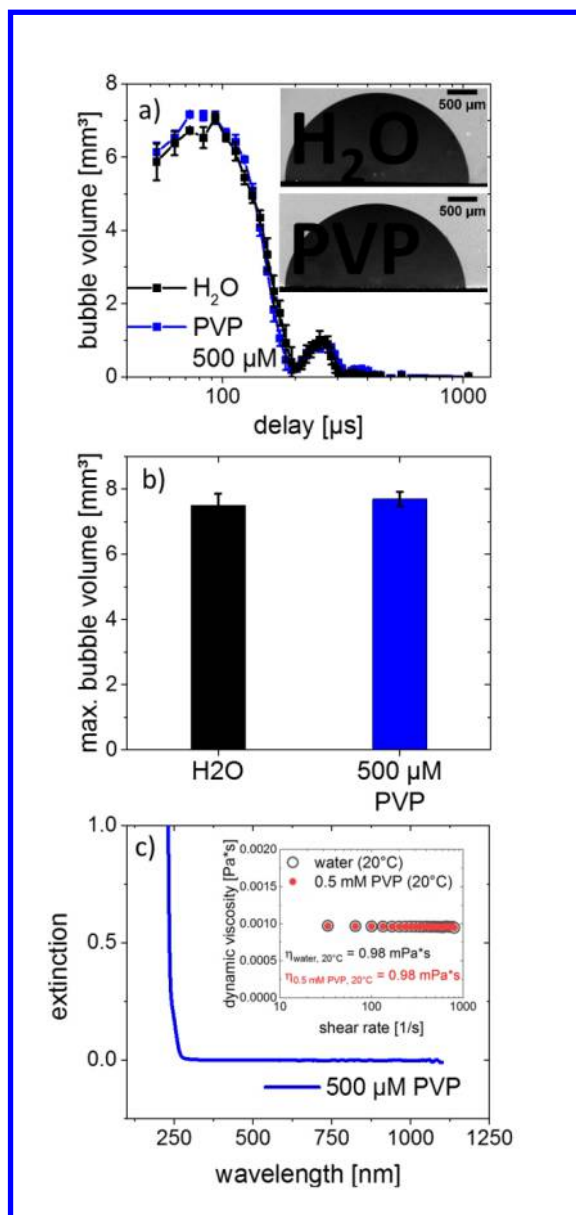


Figure 5. (a) Cavitation bubble dynamics as function of the delay from the laser impact. The PVP molecules do not affect the dynamics of the bubble. (b) Results of image analysis of the cavitation bubble at its maximum extension at  $93 \mu\text{s}$  after laser impact on the target showing no difference between pure water and  $500 \mu\text{M}$  PVP solution. (c) UV/Vis extinction spectrum of a  $500 \mu\text{M}$  PVP solution. The solution is transparent at the laser wavelength of  $1064 \text{ nm}$ . Inset: Dynamic viscosity of pure water and a  $0.5 \text{ mM}$  PVP solution.

80x170mm (300 x 300 DPI)